



Full length article

# Interaction of irradiation defects with precipitates in CuCrZr and Cu-1Fe alloys

Yi-Nan Bian<sup>a</sup>, Yan Lu<sup>a</sup>, Jian Zhang<sup>b</sup>, Bin Gao<sup>c</sup>, Wen-Bin Wang<sup>c</sup>, Wei-Zhong Han<sup>a,\*</sup><sup>a</sup> Center for Advancing Materials Performance from the Nanoscale, State Key Laboratory for Mechanical Behavior of Materials, Xi'an Jiaotong University, Xi'an 710049, China<sup>b</sup> College of Energy, Xiamen University, Xiamen 361005, China<sup>c</sup> Shaanxi Sirui New Materials Co., Ltd, China

## ARTICLE INFO

## Keywords:

Precipitate  
Irradiation  
Helium  
Void  
Interface

## ABSTRACT

In this work, we employ transmission electron microscopy and helium ion irradiation to study the interactions between the radiation-induced point defects and the incoherent/semi-coherent precipitates in CuCrZr and Cu-1Fe alloys. Both thin foil and bulk implantation were used to explore the interactions of radiation defects with interfaces. The irradiated defects show a strong interface character dependence in both implanted CuCrZr and Cu-1Fe alloys after similar level of radiation damage. Large-sized voids appear around the incoherent Cr precipitates, while no visible cavities are formed around precipitates in Cu-1Fe alloy. Interestingly, three types of semi-coherent Fe precipitates exhibit various irradiation damage mitigation mechanisms, such as twin boundaries migration, short range elements redistribution and precipitate abnormal growth, which are caused by radiation defect-mediated dislocation glide, element diffusion and mass transportation. The high sink efficiency of the incoherent precipitates trap vacancies and leads to the generation of submicron-sized voids. In contrast, the semi-coherent precipitates can regulate the motion of point defects and effectively enhance the recombination rate of vacancies and interstitials.

## 1. Introduction

A large amount of high-energy particles generated by nuclear reactions cause severe irradiation damage to reactor structural materials, resulting in degradation of both mechanical and physical properties of the materials [1–4]. Irradiation by high-energy particles (including protons, neutrons, light/heavy ions, etc.) introduces large amount of vacancies and interstitials in materials and these point defects further aggregate and evolve into dislocation loops, stacking fault tetrahedrals (SFTs), bubbles and voids [1–4]. The accumulation of irradiation defects causes hardening, embrittlement and reduction of thermal conductivity, which accelerates the degradation of material properties [4–7]. Interface engineering aims to introduction of high-density interfaces in materials as sinks for irradiation defects, which can effectively enhance radiation tolerance of materials [8–12]. The key to reducing irradiation damage is to increase the recombination/annihilation rate of point defects [8–12]. Interfaces inside the material can capture point defects generated by irradiation and accelerate the recombination of vacancies with interstitials, through which the accumulation of irradiation defects

are largely suppressed [12–14]. Materials can be strengthened by second phase particles, which also simultaneously introduce a high density of coherent, semi-coherent or incoherent interfaces, thus some of precipitate hardened materials exhibit excellent irradiation resistance, which is related to the orientation relationship and phase stability of the precipitates [15–17].

CuCrZr and CuFe are two common precipitation hardened alloys that have been extensively used for heat sink materials and lead frame structures [7,16,18]. The interfaces between precipitates and matrix in these Cu alloys are coherent, semi-coherent or incoherent, depending on the type of precipitates [19–27]. For Cu-Cr alloys, face-centered cubic (FCC) Cr-rich precipitates with size around several nanometers are coherent with FCC Cu matrix in the early stage of aging. After long time aging, FCC Cr precipitates transform into body-centered cubic (BCC) Cr precipitates, and they follow an orientation relationship (OR) of either Nishiyama–Wassermann (N-W) or Kurdjumov–Sachs (K-S) with Cu matrix [20,21,26,28]. In addition, some experiments show that these two precipitates with semi-coherent interfaces transform to incoherent precipitates with longer artificial aging [19,20,26]. For Cu-Fe alloy, the

\* Corresponding author.

E-mail address: [wzhanxjtu@mail.xjtu.edu.cn](mailto:wzhanxjtu@mail.xjtu.edu.cn) (W.-Z. Han).<https://doi.org/10.1016/j.actamat.2023.118964>

Received 19 February 2023; Received in revised form 8 April 2023; Accepted 25 April 2023

Available online 25 April 2023

1359-6454/© 2023 Acta Materialia Inc. Published by Elsevier Ltd. All rights reserved.

FCC Fe precipitate has an OR of cube-on-cube in the earlier stage of aging, which is near coherent with Cu matrix. After small deformation and subsequent artificial aging, the semi-coherent BCC Fe precipitates form and have ORs of Pitsch or K-S with the Cu matrix [27,29,30].

According to the existing irradiation studies on coherent and incoherent precipitates, different irradiation defects and special distribution characteristics are observed after radiation [31–34]. *In-situ* electron irradiation experiments of FCC Fe precipitates in Cu-1.52 wt.%Fe alloy showed that the formation of SFTs in the vicinity of the Fe particles, which only align along the  $\langle 110 \rangle$  direction [31]. Interstitial clusters form preferentially in the immediate vicinity of Fe particles and cause uneven distribution of vacancies [31]. As a consequence, SFTs are formed unevenly around the Fe particles [31,35]. But in electron irradiated pure Cu, SFTs distribute along the  $\langle 100 \rangle$  direction [35]. Preferential nucleation of SFT along the  $\langle 100 \rangle$  direction occurs directly related to the enrichment of vacancies in the stress field of stair rod dislocations composing the SFT. In addition to the directional distribution of defects, the precipitates lost coherence because of phase transformation or elemental diffusion [17,36–38]. Interfacial changes and elemental diffusion do not only occur in irradiated Cu alloys, but also occurs in some oxide dispersion strengthened (ODS) steels [33,34,39]. The incoherent interface in OSD steels absorbs vacancies, which further aggregate to form cavities or mix with He ions to form He bubbles at interface [33,34,39]. The precipitates with different ORs with matrix have different features in influencing the defect motion and recombination behaviors of point defects. However, there is no direct comparative study of the interactions between irradiation defects and the precipitates with different ORs under similar irradiation conditions.

In this study, we aim to understand the role of the coherent, semi-coherent and incoherent precipitates of Cu alloys in the development of radiation damage, including the evolution of the precipitates after irradiation and the types and characteristics of irradiation defects. To this end, CuCrZr and Cu-1Fe alloys are selected as model materials. As-aged CuCrZr alloy contains fully incoherent Cr precipitates. As-aged Cu-1Fe alloy have four types of Fe precipitates, for example, one type of coherent precipitate and three kinds of semi-coherent precipitates [28,40,41]. These samples can be easily prepared by solid solution and artificial aging of bulk CuCrZr and Cu-1Fe alloys. Both helium (He) ions implantation and thin foil irradiation (He ions penetrate the sample) were used to bombard CuCrZr and Cu-1Fe samples to clarify the interaction of radiation defects with coherent, semi-coherent/incoherent precipitates in a wide range of radiation damage.

## 2. Experimental procedures

As-aged samples with suitable size of precipitates were obtained by solid solution and artificial aging of Cu-0.87 wt.%Cr-0.15 wt.%Zr (CuCrZr) and Cu-1 wt.%Fe alloys (Cu-1Fe) produced by Shaanxi Sirui New Materials. No artificial addition of other elements, the total content of impurity elements other than the main elements is below 0.1%. The bulk samples were sealed in quartz tube with pure Argon protection and solutionized at 1150 °C for 48 h following water quenching. CuCrZr and Cu-1Fe alloys were aged at 750 °C for 10 h and at 700 °C for 8 h with a vacuum of about  $2 \times 10^{-2}$  pa, respectively. The solution-treated Cu-1Fe thin foil samples were cut from solutionized bulk sample for irradiation test. The bulk samples were grounded and polished to a mirror surface. The thin foil samples with a diameter of 3 mm were grounded to about 50  $\mu$ m in thickness and then electrolytic polished using a solution of one part nitric acid and three parts methanol at  $-30$  °C using a voltage of 30 V.

Irradiation was performed on these two types of samples using He ions with the energy of 200 keV at 400 °C by using a NEC Implanter to an ion fluence of  $1 \times 10^{17}$  ions/cm<sup>2</sup> with a flux rate of  $1.52 \times 10^{13}$  ions/cm<sup>2</sup>/s. He beam was tuned 7° off compared to the normal of samples to avoid channeling effect. The radiation damage (in units of displacement per atom, dpa) and the He concentration as a function of depth from the

top surface can be estimated using the Stopping and Range of Ions in Solids (SRIM) [42] with threshold displacement energy of 29 eV for Cu, 44 eV for Fe, 60 eV for Cr and 40 eV for Zr [43]. Fig. 1 shows the variation of dpa (black line) and the He concentration (red line) with depth from the sample surface in thin foil and bulk Cu-1Fe, as illustrated in Fig. 1(a) and (b). Irradiation damage and He concentration of CuCrZr alloy are similar to that of Cu-1Fe alloy.

Precipitate structures and radiation defects of samples before and after radiation were characterized using a JEOL 2100F (200 kV) transmission electron microscope (TEM). In order to study the radiation defects as a function of depth, thin foils were cut at different position in bulk implanted sample using a focused ion beam (FIB, Helios 600), as illustrated in Fig. 1(b). The TEM sample of selected depth  $D$  means that it spans from  $D-50$  to  $D+50$  nm. The ion beam current was reduced to 46 pA for the final polishing to minimize possible FIB-induced surface damage. Two-beam diffraction contrast and defocus imaging were used to study the radiation defects. All cavities were observed with a defocus of  $-2$   $\mu$ m.

The diameter of different Fe precipitates in Cu-1Fe is measured in the bright-field or dark-field imaging with zone axis of  $[011]_{\text{Cu}}$ , respectively. The number density of Fe precipitates were counted based on around 100 the bright-field or dark-field images with zone axis of  $[011]_{\text{Cu}}$ . Precipitates with cube-on-cube OR are counted using bright-field images. Precipitates with ORs of Pitsch, N-W and K-S are counted on dark-field images. The thicknesses of TEM samples are about 100 nm. The diameter and number densities of the precipitates in different samples were all measured and compared before and after irradiation.

## 3. Results

### 3.1. Initial microstructures and irradiation defects in thin foil CuCrZr

During the aging, since the content of Cr in CuCrZr exceeds the equilibrium concentration, the Cr precipitates nucleate and grow up. Fig. 2(a) and (b) show the bright-field TEM images and the selected area diffraction pattern (SADP) of the as-aged CuCrZr before and after irradiation, viewed with zone axis of  $[111]_{\text{Cr}}$  and  $[011]_{\text{Cu}}$ . Unlike the reported coherent or semi-coherent Cr precipitates [21,23,25], the diffraction spots of Cu matrix and the Cr precipitates do not show a fixed OR, which means the Cr precipitates are fully incoherence with Cu matrix. The Cr precipitates display various shapes, as shown in Fig. 2(a). With extensive analysis of the as-aged CuCrZr samples, no CuZr<sub>4</sub> or CuZr<sub>5</sub> phases [44,45] are observed and only the pure Cr precipitates [19,26].

Fig. 2(b) to (f) display the defect structures in CuCrZr after thin foil irradiation. According to SRIM simulations, the average radiation damage of CuCrZr thin foil is about 1.2 dpa and the He concentration is zero. Large voids (vacancies cluster) with size of 100 nm are attached to the Cr precipitates, as marked in Fig. 2(b). Randomly distributed SFTs can be seen in Cu matrix, while no cavities and interstitial clusters are observed in Fig. 2(c). Fig. 2(d) shows a large void attached to a micron-sized Cr precipitates. Fig. 2(e) and (f) highlight the irradiation defects in both Cu and Cr precipitate. There is no SFT in the Cu matrix around the Cr precipitate. The micron-scale void almost separates the Cr precipitate from the Cu matrix, which is a result of accumulation of a large number of vacancies at Cu-Cr interface. Meanwhile, a large number of interstitial dislocation loops are observed in the Cr precipitate in Fig. 2(f).

### 3.2. Depth-dependent radiation defects in bulk implanted CuCrZr

To analyze the influence of incoherent precipitates on the evolution of radiation defects in bulk CuCrZr, thin foils were cut at different relative depths from the sample surface. Specifically, we selected nine thin foils with a depth between 0 and 5000 nm from the surface and divided them into two categories: the He implanted region and the point defect diffusion zone (beyond the limit of He ion transmission). The

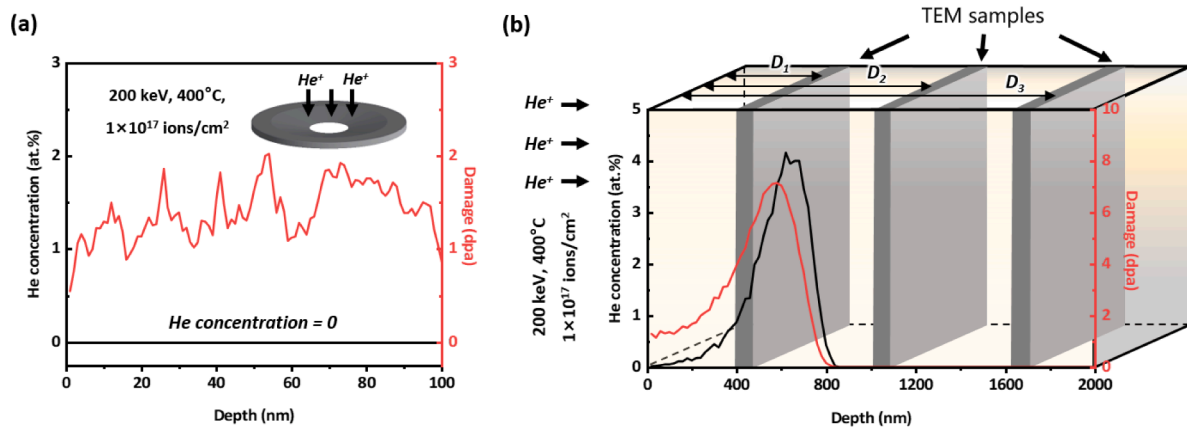


Fig. 1. Schematic of He implantation in thin foils and bulk samples using a He ion energy of 200 keV to a fluence of  $1 \times 10^{17}$  ions/cm<sup>2</sup> at 400 °C. He ion beam was tuned to implant near perpendicular ( $7^\circ$ -off) to the surface of thin foils and the top surface of bulk samples. (a) He concentration (black line) and damage distribution (red line) in irradiated thin foil. (b) He concentration (black line) and damage distribution (red line) in irradiated bulk sample. The slices represent TEM samples that were cut at certain radiation depths  $D$  that means the sample is cut from a depth of  $D-50$  to  $D+50$  nm.

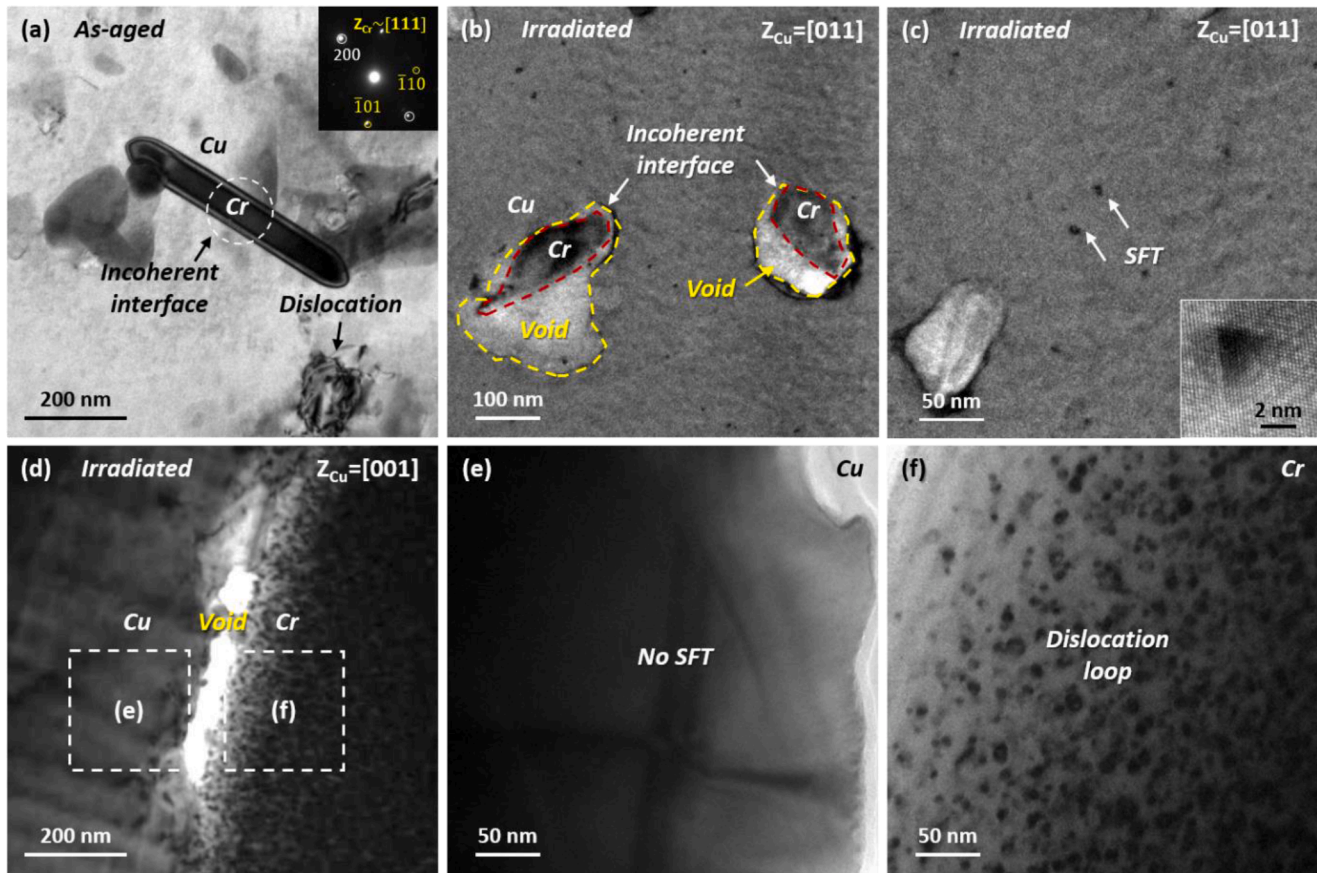
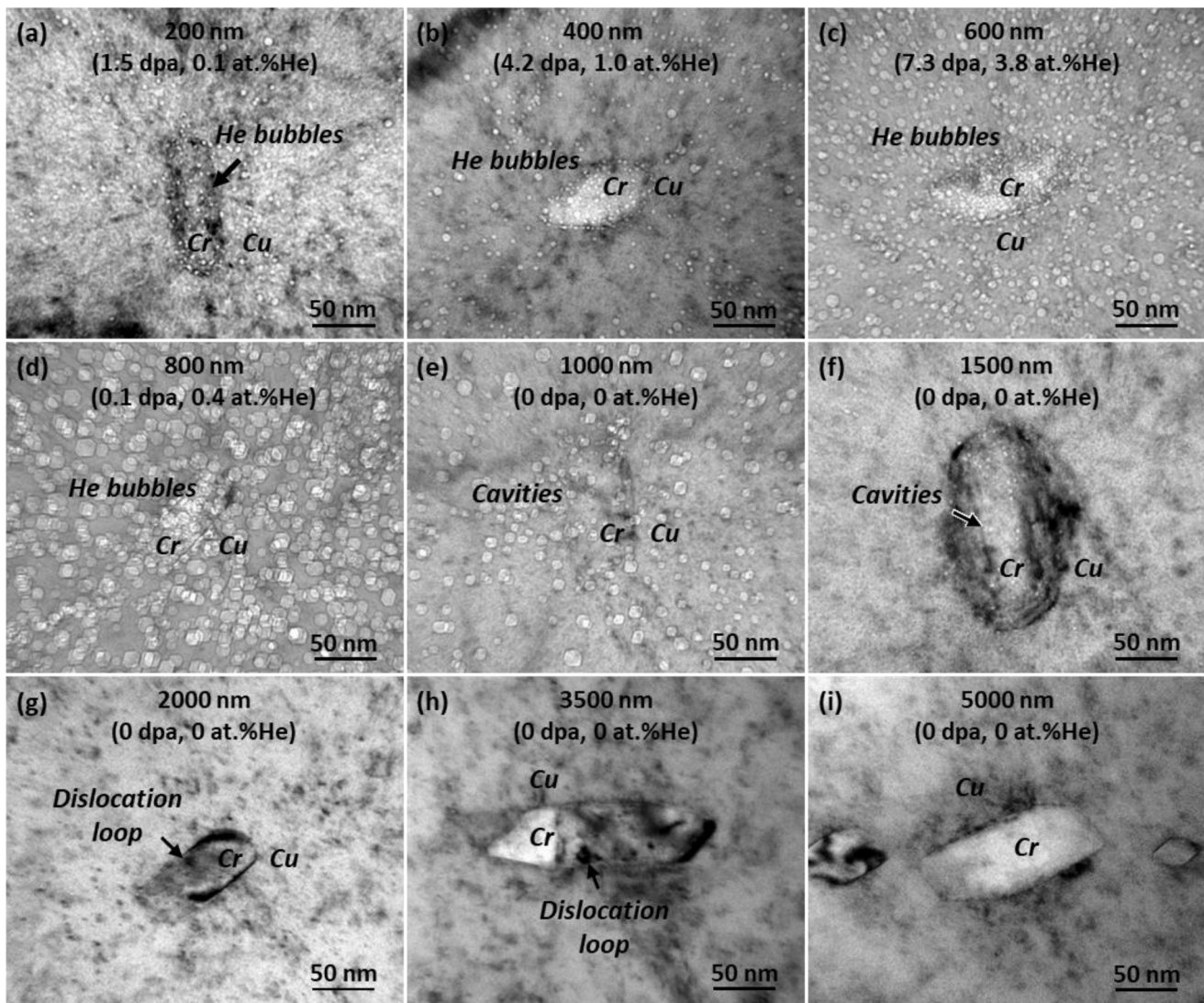


Fig. 2. Microstructures in the as-aged and irradiated CuCrZr alloy. (a) Bright-field TEM images and SADPs of BCC Cr precipitate in as-aged CuCrZr. (b) and (c) TEM images taken near [110] beam direction. Irradiation-induced voids (circled by the yellow dash line) are attached to the Cr precipitates (circled by the red dash line). Some SFTs randomly distribute in Cu matrix. (d) Typical TEM image near a micron-sized Cr precipitate. (e) and (f) are enlarged images corresponding to the white rectangles in (d).

range of radiation damage in the He implanted region varies with depth from 0 to 7.4 dpa and the He concentration continues to increase from 0 to 4.3 at.%. Since the He concentration is not zero, the observed cavities are He bubbles. The number densities and diameter distributions of He bubbles, cavities and dislocation loops are shown in Fig. S1.

Fig. 3(a) and (d) show the distribution of defects in He implanted region. At  $D = 200$  nm and 400 nm, only He bubbles are visible and no

SFTs or dislocation loops are observed. The sizes of He bubbles are  $3.3 \pm 0.7$  nm and  $5.0 \pm 1.6$  nm, respectively. More He bubbles are distributed around the Cr precipitate (Fig. 3(c)). At  $D = 600$  nm and 800 nm, the density and size of He bubbles increase. With increasing irradiation damage and He concentration, He bubbles are always preferred to attach to the Cr precipitates. Fig. 3(d) shows the radiation defects in the bulk



**Fig. 3.** Radiation defects in bulk CuCrZr after He implantation at depths of (a)  $D = 200$  nm, (b)  $D = 400$  nm, (c)  $D = 600$  nm, (d)  $D = 800$  nm, (e)  $D = 1000$  nm, (f)  $D = 1500$  nm, (g)  $D = 2000$  nm, (h)  $D = 3500$  nm and (i)  $D = 5000$  nm. All images were taken with under focus of  $2 \mu\text{m}$ .

CuCrZr alloy at  $D = 800$  nm. The irradiation damage and He concentration are 7.3 dpa and 3.8 at.%. A high density of He bubbles overlaps each other in the Cu matrix and at the Cr precipitate. He bubbles in the Cr precipitates have an average size of  $2.1 \pm 0.4$  nm, much smaller than the He bubbles ( $11.3 \pm 1.6$  nm) in Cu matrix, as shown in Fig. S2. Because of higher surface energy ( $\gamma_{\text{Cr}} = 2.20 \text{ J/m}^2$  for Cr,  $\gamma_{\text{Cu}} = 1.77 \text{ J/m}^2$  for Cu) and high migration energy ( $E_{\text{Cr}}^m = 0.95 \text{ eV}$  for Cr vacancy,  $E_{\text{Cu}}^m = 0.72 \text{ eV}$  for Cu vacancy) of vacancies in Cr than that in Cu [46–50], the spherical He bubbles are expected to be smaller in Cr than in Cu. A large number of He bubbles still accumulate around Cr precipitate, but the size of the He bubbles increases significantly.

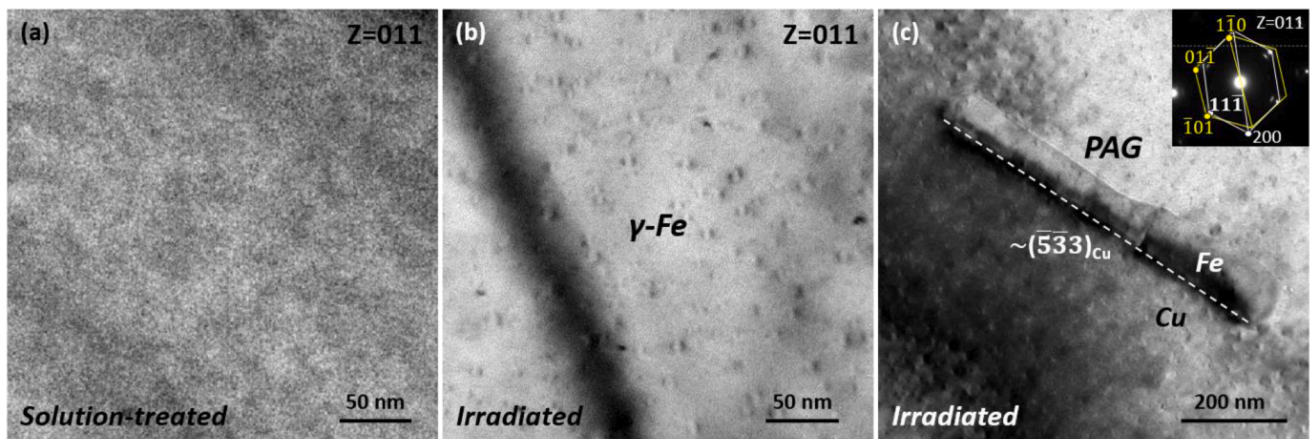
According to the SRIM simulation, He ions implant to a maximum depth of 1000 nm. The radiation damage and He concentration in the region beyond 1000 nm should be zero. However, some irradiation-induced point defects could migrate into deeper region. We also performed characterizations in the region at a depth from  $D = 1000$  to 5000 nm. The migration of Cu vacancies ( $E_{\text{Cu}}^m = 0.72 \text{ eV}$ ) is more difficult than interstitials ( $E_{\text{Cu}}^m = 0.084 \text{ eV}$ ) [49,51], therefore we observed the separated vacancy migration region and interstitials migration region. Fig. 3 (e) and (f) show the distribution of defects in the vacancy migration region at  $D = 1000$  nm and 1500 nm. Similar with the region of low irradiation damage and He concentration, cavities (likely containing He

but cannot be confirmed) attached to the Cr precipitate as well. The sizes of cavities are  $8.6 \pm 2 \text{ nm}$  and  $3.1 \pm 0.7 \text{ nm}$  at  $D = 1000$  nm and 1500 nm, respectively. The density and size of cavities decrease dramatically with increasing depth, as shown in Fig. S1. Fig. 3(g) and (h) display the radiation defects in the interstitials migration region at  $D = 2000$  nm and 3500 nm. The black dots are interstitial clusters, and the number density of dots smaller at  $D = 3500$  nm than that at 2000 nm. No radiation defects are observed at  $D = 5000$  nm, as shown in Fig. 3(i).

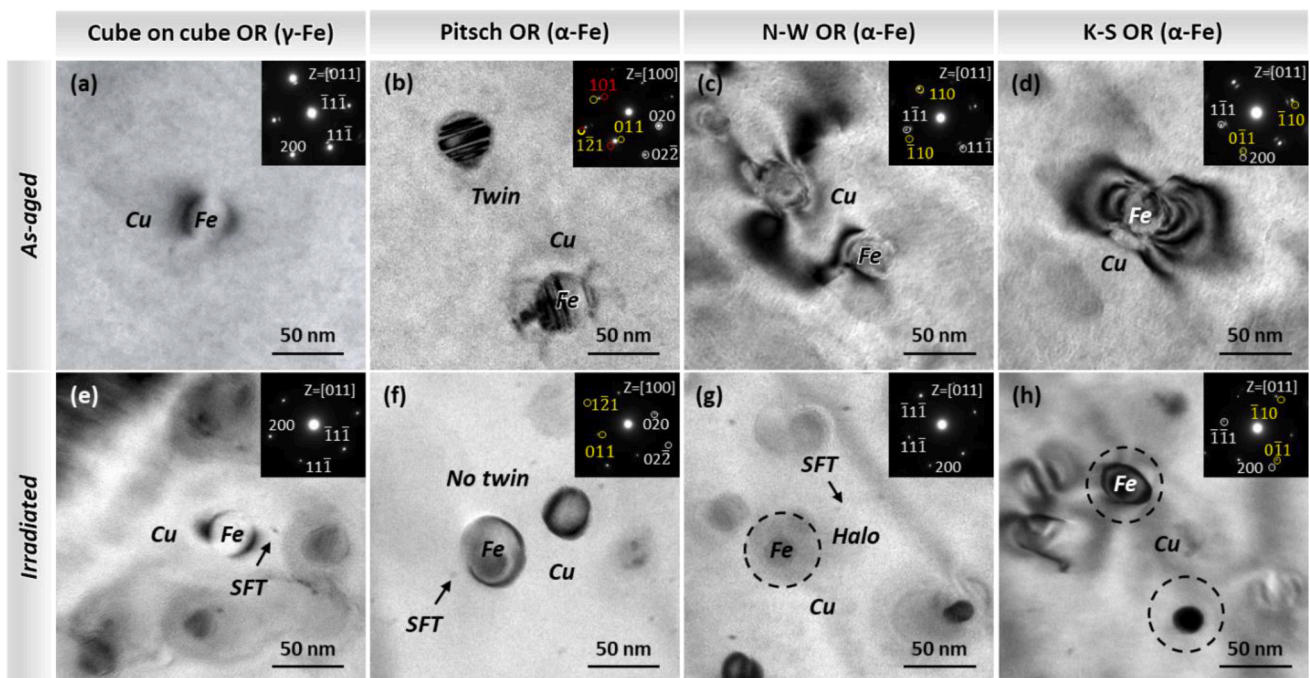
### 3.3. Initial microstructures and irradiation defects in Cu-1Fe

Fig. 4 show the solution-treated Cu-1Fe sample before and after He irradiation. There are no obvious precipitates in solution-treated Cu-1Fe (Fig. 4(a)). Abundant FCC Fe precipitates with an average size of 10 nm are uniformly embedded in Cu matrix after irradiation (Fig. 4(b)). Fig. 4 (c) shows a lath-like precipitate with K-S OR after irradiation. The facet plane of precipitate is approximately  $(\bar{5}\bar{3}\bar{3})_{\text{Cu}}$ . This observation indicates that irradiation accelerates the precipitate abnormal growth.

Fig. 5(a) to (d) displays the four typical Fe precipitates formed in Cu-1Fe after artificial aging. Fig. 5(a) shows a coherent FCC Fe precipitate ( $[100]_{\text{Cu}}//[100]_{\text{Fe}}$ ,  $[110]_{\text{Cu}}//[110]_{\text{Fe}}$ ,  $(1\bar{1}\bar{1})_{\text{Cu}}//(\bar{1}\bar{1}\bar{1})_{\text{Fe}}$ ) embeds in the Cu matrix [40]. The bean contrast of the spherical precipitate is a



**Fig. 4.** Microstructures of solution-treated Cu-1Fe alloy (a) and after thin foil irradiation (b) and (c). (b) Precipitates with bean contrast distribute evenly in Cu. (c) Lath-like Fe precipitate with K-S OR forming with facet plane of near  $(\bar{5}33)_{\text{Cu}}$ .



**Fig. 5.** Microstructures of the as-aged Cu-1Fe alloy before (a to d) and after He irradiation on thin foil (e to h). (a) to (h) are the bright-field TEM images and SADPs of four kinds of Fe precipitate in the as-aged and irradiated thin foil Cu-1Fe alloy. (e) to (h) show the distribution of SFTs and variation of precipitates in thin foils after He irradiation. (f) Twins disappeared in the precipitates with Pitsch OR after irradiation. (g) Halo is formed around some precipitates with N-W OR. (h) Precipitates with K-S OR are remained stable, but some of them grow up with facet planes.

common feature of coherent precipitates in Cu alloy [36,37]. Fig. 5(b) shows a BCC Fe precipitate with Pitsch OR ( $[011]_{\text{Cu}}/[111]_{\text{Fe}}$ ,  $(200)_{\text{Cu}}/(\bar{1}01)_{\text{Fe}}$ ,  $(022)_{\text{Cu}}/(\bar{1}21)_{\text{Fe}}$ ) viewed along  $[001]_{\text{Cu}}$  [28,41]. BCC twins are formed in the precipitates with Pitsch OR. Figs. 5(c) and (d) shows the spherical Fe precipitates with N-W OR ( $[011]_{\text{Cu}}/[001]_{\text{Fe}}$ ,  $(11\bar{1})_{\text{Cu}}/(\bar{1}10)_{\text{Fe}}$ ,  $(422)_{\text{Cu}}/(\bar{1}10)_{\text{Fe}}$ ) and K-S OR ( $[011]_{\text{Cu}}/[111]_{\text{Fe}}$ ,  $(11\bar{1})_{\text{Cu}}/(\bar{1}01)_{\text{Fe}}$ ,  $(422)_{\text{Cu}}/(\bar{1}21)_{\text{Fe}}$ ) [28,41], respectively. We obtained the four kinds of spherical precipitates after one-time artificial aging. The diameters of the four precipitates are approximately similar, around 30 nm. The high resolution TEM images of the four precipitates in the as-aged Cu-1Fe are shown in Fig. S3.

Figs. 5(e) to (h) show the defects structure and precipitates after thin foil irradiation. The FCC Fe precipitate still maintains the coherent feature (Fig. 5(e)). SFTs with an average size of about 3 nm are uniformly distributed in the Cu matrix and no cavities are observed in these

defocused images. The bright-field, dark-field and high magnification TEM images of SFTs near the Fe precipitates are shown in Fig. S4. These observations confirm the triangle-shaped irradiation defects are SFTs. Twins are disappeared in the two precipitates with Pitsch OR after irradiation (Fig. 5(f)) and their diameter is larger than the as-aged precipitates (Figs. 4(b)). As shown in the Fig. S5, the twin structures remain stable after long period annealing, hence the detwinning is caused by ion irradiation.

Fig. 5(g) displays a precipitate with a halo feature. The Cu/Fe interface is blurred and the diffraction spot of the precipitate cannot be obtained, which means that the original OR has been completely destroyed with short range Fe elements redistribution. Fig. 6(a) and (b) display the energy spectrum analysis of the halo region, which is caused by the diffusion of Fe solutes from precipitates during irradiation. Fig. 5 (h) shows the two circled precipitates with K-S OR. One of the faceted

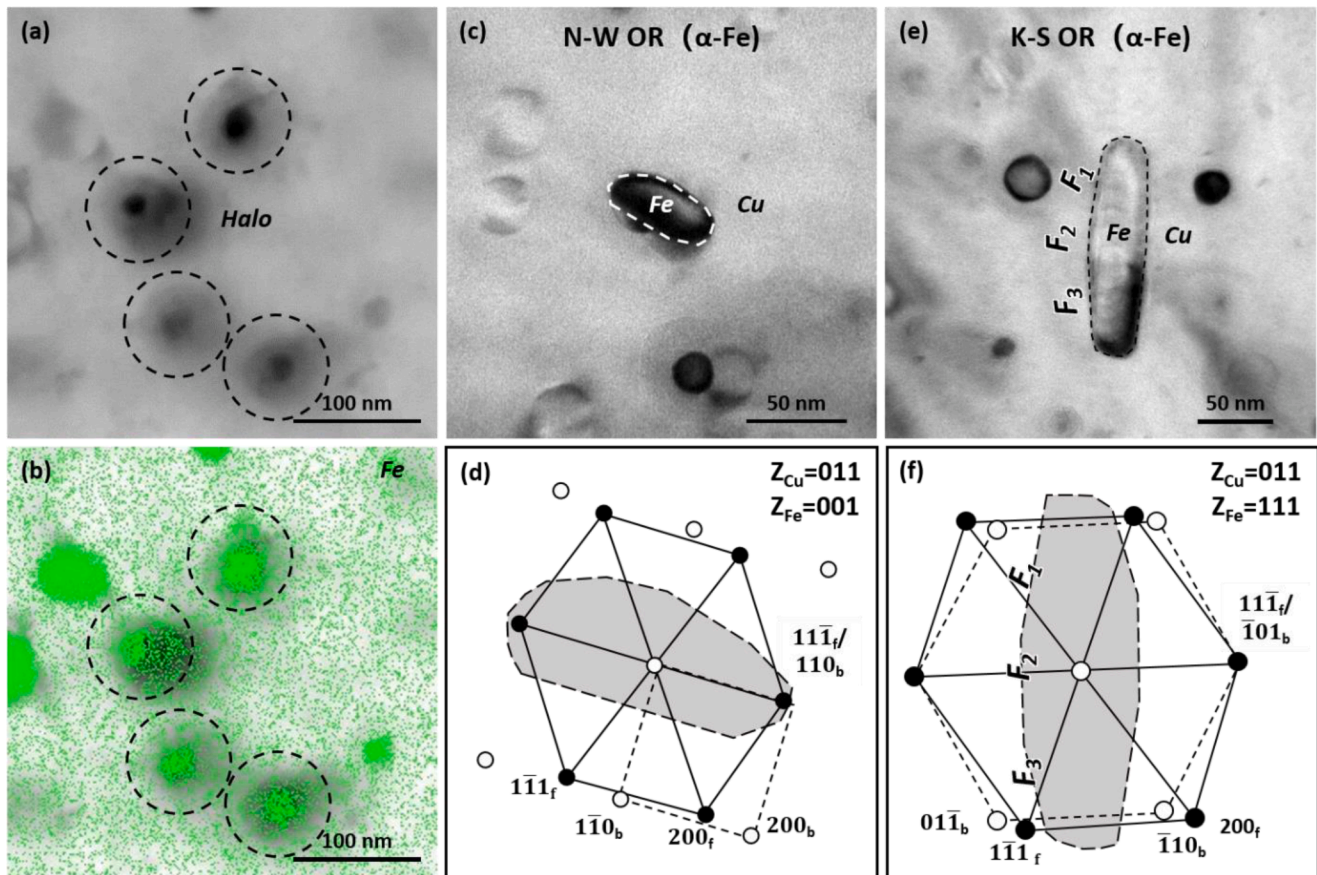


**Fig. 6.** Microstructure of precipitates in Cu-1Fe after thin foils He irradiation. (a) STEM image showing the precipitates with halo. (b) EDS mapping of precipitate in (a). (c) and (e) are precipitates with N-W OR and K-S OR. (d) is the sketch of the precipitate in (c) with its  $[011]_{\text{Cu}}/[001]_{\text{Fe}}$  diffraction pattern superimposed. (f) is the sketch of the precipitate in (e) with its  $[011]_{\text{Cu}}/[111]_{\text{Fe}}$  diffraction pattern.

precipitates has a diameter of 50 nm, while the other one remains spherical, similar to the diameter before irradiation. There is no SFT around precipitates with K-S OR.

In addition to the observation above, there are also a small number of cases where precipitate abnormal growth occurs in the precipitates. Fig. 6(c) shows the precipitate with N-W OR with a broad bean contrast. According to the comparison of the bright and dark field images, the faceted plane of the precipitate is  $\{011\}_{\text{Fe}}$ . Fig. 6(e) shows the lath-like precipitate with K-S OR, and the faceted plane  $F_1$  and  $F_2$  are  $(533)_{\text{Cu}}$  and  $(11\bar{1})_{\text{Cu}}$ . Similarly, the facets of Cr precipitates in CuCr alloy are  $\{533\}_{\text{Cu}}$  and  $\{111\}_{\text{Cu}}$  [23,25,52]. The faceted plane  $F_1$  of the precipitate is highly similar to one of the abnormal growth precipitate in solution-treated samples, which may be an intrinsic feature of the BCC Fe precipitate.

The number density and diameter distributions of the four types of precipitates in the as-aged and after thin foil irradiation are shown in Fig. 7. In as-aged sample, the diameters of the four precipitates are similar, all around 30 nm, while the density of the FCC Fe precipitate is the highest and the densities of the three BCC Fe precipitates are similar. The special density distribution means that the spherical FCC Fe precipitate forms first during artificial aging, and then gradually transforms into BCC Fe precipitate with three different ORs. In irradiated thin foil sample, the diameter of FCC Fe has no change but the number density has little increase compared with the as-aged samples. The number density of the precipitates with Pitsch OR keeps unchanged as well, but the size increases. The yellow arrow in Fig. 7 points the number density of the abnormal growth precipitate with N-W OR. No spherical N-W precipitates were found, and a large number of precipitates with halo were observed. By comparing the number density of precipitates of N-W OR before and after irradiation, it can be determined that precipitates

with halo are the typical character of precipitates with N-W OR after irradiation. After irradiation, not only the shape but also the diameter has obvious change for these coherent and semi-coherent Fe precipitates. A large portion of the precipitate with K-S OR are spherical or nearly spherical with a continuous size distribution of about 50 nm, and a small portion of the lath-like precipitates have a long axis of about 100 nm. Therefore, the diameter variation of the precipitate with K-S OR is larger than that of other precipitates, as indicated in Fig. 7.

#### 3.4. Radiation defects in bulk implanted Cu-1Fe

To analyze the effect of depth-dependent irradiation defects in Cu-1Fe and their interaction with Fe precipitates, thin foils were cut at depths from  $D = 0$  to  $D = 2000$  nm relative to the sample surface. Similar to the CuCrZr bulk samples, we divided them into two regions: the He-implanted region and the point defect diffusion region (beyond the maximum He-implanted depth). The radiation damage in the He implanted region ranges from 0 to 7.1 dpa, and the He concentration increased continuously from 0 to 4.1 at.%.

Fig. 8 shows the accumulation of He bubbles around the three kinds of Fe precipitates in the He-implanted region. The size of the He bubbles increases with depth. At  $D = 600$  nm, the peak irradiation damage (7.1 dpa) and He concentration (3.7 at.%), the semi-coherent interfaces and the twins are survived. The diameter and density of He bubbles increase with depth in this region. The radiation damage and He concentration in the region beyond 1000 nm should be zero, hence the deeper regions are He free. Fig. 9 shows the radiation defects at  $D = 1500$  nm and 2000 nm for the bulk implanted Cu-1Fe. The observation of cavities (likely containing He but cannot be confirmed) at  $D = 1500$  nm indicates that the

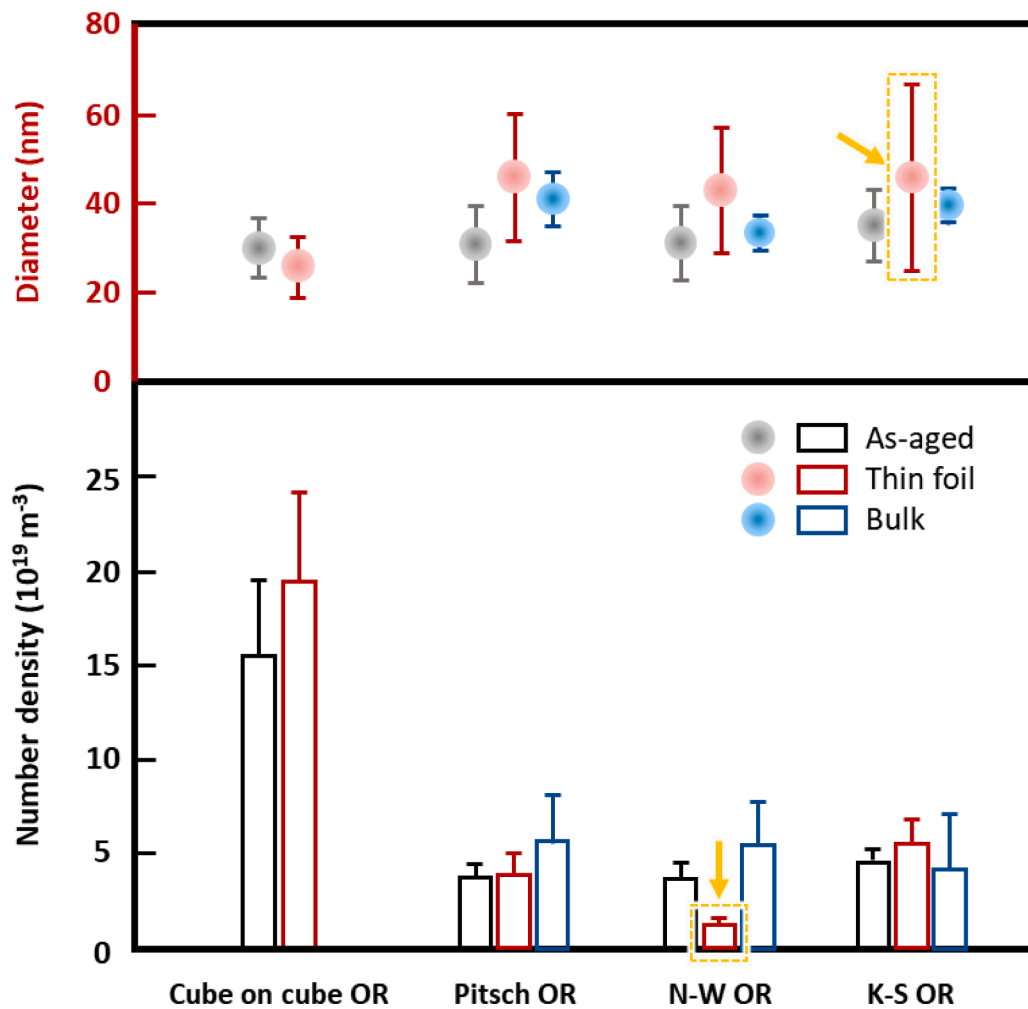


Fig. 7. The number density and diameter distributions of the four types of precipitates in the as-aged sample, after thin foil irradiation and bulk implantation. Precipitates with cube on cube OR in bulk implanted sample are not counted due to their poor contrast.

radiation-induced vacancies and interstitials are mobile and spread beyond the limits of the He implanted region, forming cavities ( $2.7 \pm 0.6$  nm) and interstitial clusters attached to the Fe precipitates. No radiation defects are detected at  $D = 2000$  nm (Fig. 9(f)). Unlike the thin foil irradiation, the Fe precipitates in bulk implanted sample almost maintain the same diameter and number density as the as-aged samples, as shown in Fig. 7. Due to severe interference between irradiation defects and the FCC Fe precipitates, we did not capture these precipitates in the bulk implanted Cu-1Fe.

## 4. Discussion

### 4.1. Interaction between Cr precipitates and irradiation defects

The precipitate-matrix interfaces are sinks, which have a strong bias on the segregation of point defects in irradiation [8,9,13,14]. As shown in Fig. 10(a), large-size voids are distributed near Cr precipitates. Only a small amount of 4 nm SFTs are formed in Cu, and no cavities are observed. The incoherent interface acts as strong sink of point defects and attracts a large number of vacancies to accumulate near the interface, thus forming micron-scale void. The incoherent interface between Cr precipitate and Cu is completely separated, while there are only some tiny dislocation loops in Cr precipitate.

According to SRIM simulations, the irradiation damage is similar for thin foil irradiation (1.2 dpa) and the sample at  $D = 200$  nm (1.5 dpa) in bulk implantation, but there is no He in thin foil irradiated sample.

Therefore, void forms in the He-irradiated thin foil sample, but He bubbles form in the bulk implanted sample. During thin foil irradiation, the top and bottom free surfaces have a marked effect on the migration of point defects, which could attract the mobile interstitials from the center to free surfaces. Hence precipitate-vacancies interactions dominate in thin foil irradiation. In contrast, in bulk irradiated sample, except at the  $D < 100$  nm region, the surface sink effect is negligible. The precipitates are largely interacting with both interstitials and vacancies. This difference causes the formation of different defect structures in two types of irradiation. As shown in Figs. 2 and 3, SFTs and large-size voids at precipitate are produced in the thin foil irradiation, while there are no SFTs in the bulk implanted sample, and only He bubbles form.

Due to the strong surface sink effect in the thin foil irradiation, the Cu interstitials ( $E_{Cu}^m = 0.084$  eV) easily migrate to the sample free surface, while the vacancies ( $E_{Cu}^m = 0.72$  eV) are largely trapped in the thin foil and cluster into SFTs or voids [49,51]. Since Cu point defects are more mobile than the point defects in Cr, Cu vacancies move to the Cu-Cr interface and aggregate into voids, as shown in Figs. 10(a) and 12(a). Nano-scale void continues to grow and finally separate the incoherent interface. A fraction of vacancies are remained in the Cu matrix and aggregate into SFTs. Since the concentration of vacancies is much higher than the interstitials, large interfacial Cu voids are produced around Cr precipitate in Fig. 10(a).

Fig. 10(b) shows the distribution of various irradiation defects in bulk implanted CuCrZr. At  $D = 200$  nm, the vacancies gather around the incoherent interface and bind with He atoms to form He bubbles. With

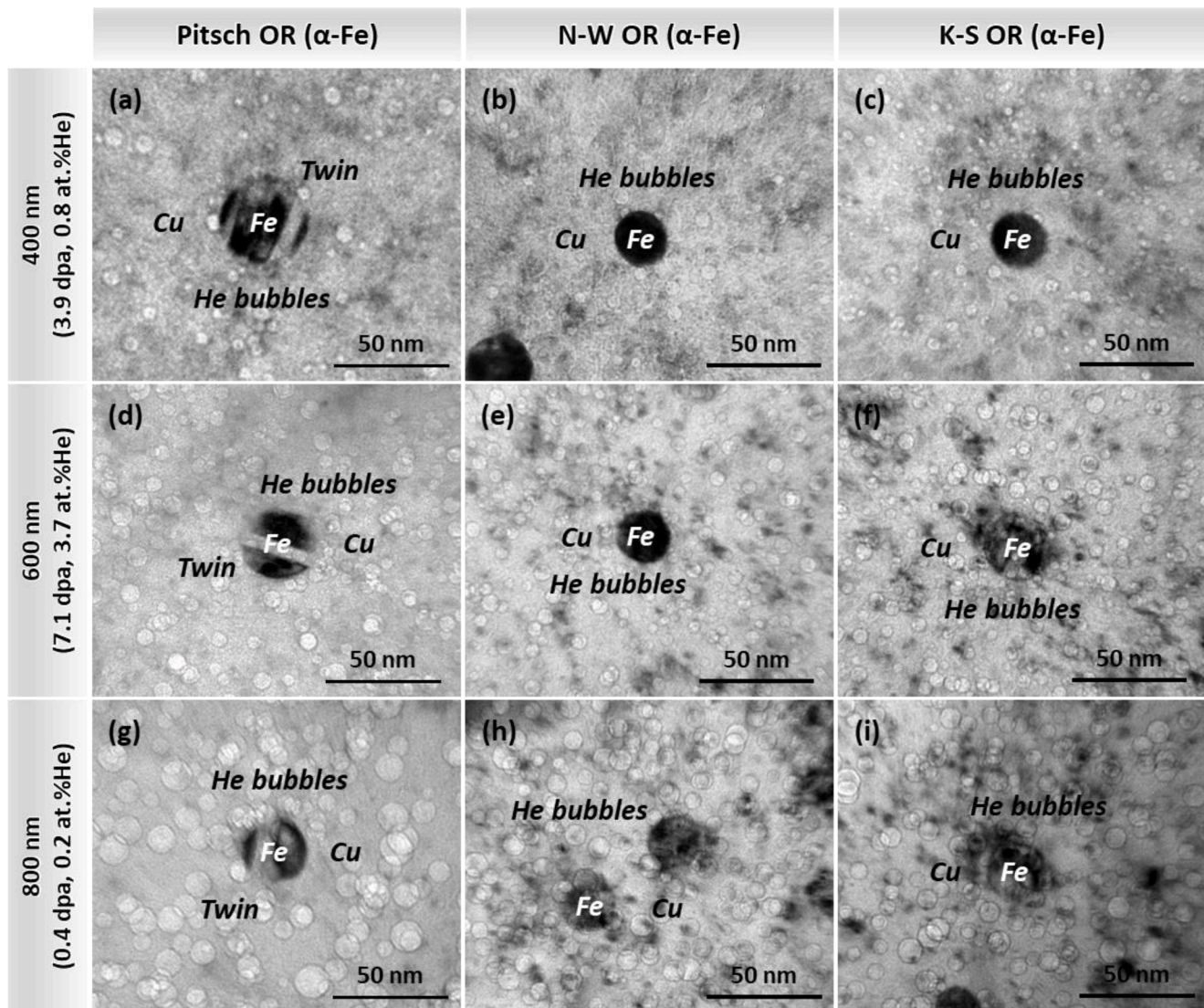


Fig. 8. Radiation defects in Cu-1Fe alloy after bulk He implantation at depths of  $D = 400$  nm,  $D = 600$  nm and  $D = 800$  nm. The images showing the interaction of Fe precipitates with He bubbles. All images were taken with under focus of  $2 \mu\text{m}$ .

the increase of depth, the size and number density of He bubbles increase significantly, and the segregation of He bubbles near Cr precipitates remain unchanged. For the region beyond the He implanted range (zero irradiation damage and He concentration), faceted cavities are also observed around the Cr precipitates. This means vacancies can diffuse beyond the He implanted region. Small black dotted clusters are also observed in region with  $D > 1000$  nm due to the faster migration of interstitials during irradiation. In this case, interstitial loops are observed around the precipitates and in the Cu matrix.

The above analysis demonstrates that the significant influence of free surface and incoherent precipitates on the dynamic evolution of radiation defects and their clustering behaviors. There are no detectable elemental diffusion around Cr precipitate in CuCrZr after irradiations, which is due to the positive heat of mixing between Cu and Cr (18.3 kJ/mol) [53].

#### 4.2. Interaction between Fe precipitates with irradiation defects

Unlike the incoherent Cr precipitates, the coherent and semi-coherent Fe precipitates exhibit completely different interacting behaviors with irradiation defects. Fe precipitates in bulk implanted sample have little changes. The diameter, number density and

characteristics of precipitates are almost the same as those of as-aged samples. However, under thin foil irradiation, they have obvious changes because of the interaction between the high density vacancies and precipitates. Fig. 11 summarizes the variation of precipitates and the typical radiation defects formed in irradiated Cu-1Fe.

The FCC Fe precipitate in Cu-1Fe still maintains a bean-like contrast with no significant change in diameter after irradiation. Due to low sink efficiency of interfaces associated with coherent precipitates, the interaction between precipitates and vacancies is weak. The lattice constant ( $a_{\text{Fe}} = 0.364$  nm [54]) of FCC Fe is slightly larger than FCC Cu ( $a_{\text{Cu}} = 0.361$  nm [55]), which produces a weak tensile stress field around the FCC Fe precipitates, however, irradiation induced interstitials are more likely attracted by the sample free surface, as illustrated in Fig. 12(b). After irradiation, the density of FCC Fe precipitate increases slightly compared to that before irradiation (Fig. 7), which means additional FCC Fe precipitates form during irradiation. In addition, no voids were observed in thin foil irradiated Cu-1Fe, which is different from the irradiation response of pure Cu or Cu/Ag nanocomposites [13,56]. Fe interstitials tend to combine with Cu vacancies, thus reducing the possibility of void formation [57].

The semi-coherent precipitate has distinct impact on the evolution of irradiation defects. The precipitates with Pitsch OR are unstable during

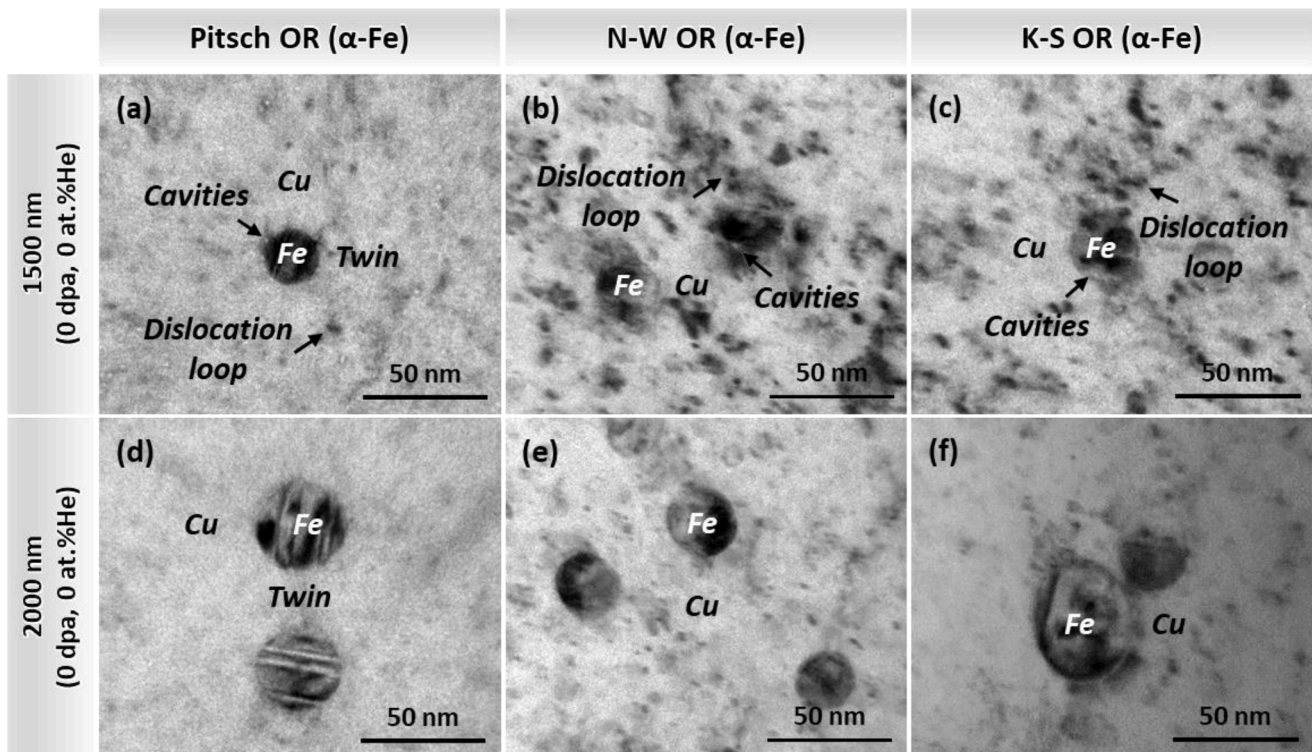


Fig. 9. Radiation defects in Cu-1Fe alloy after bulk He implantation at depths of  $D = 1500$  nm and  $D = 2000$  nm. All images were taken with under focus of  $2 \mu\text{m}$ .

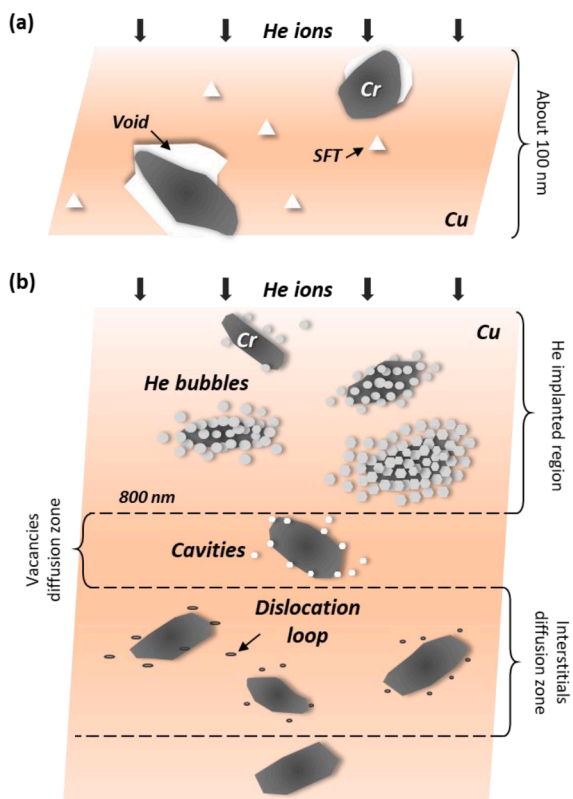


Fig. 10. Schematic of the radiation-induced defects distribution in the irradiated CuCrZr alloy (a) thin foils irradiation and (b) bulk implantation.

thin foil irradiation, for example, twin structures are disappeared, and the precipitates show abnormal growth, as illustrated in Fig. 12(b). Similar twin boundaries (TBs) migrations were also observed in

irradiated Cu and Ag [58,59]. Irradiation-induced vacancies tend to cluster at TBs and produce twin dislocation loops, which trigger TBs migration [60]. The disappearance of TBs in irradiated Fe precipitates indicates the migration of BCC TBs owing to the interaction between irradiation-induced vacancies with twins in Fe precipitates under thin foil irradiation. The abnormal precipitate growth is caused by the attraction of Fe interstitials at interface. Under thin foil irradiation, a large amount of Cu interstitials migrate to free surface, while vacancies are enriched around the precipitates. In this case, the knock-out Fe interstitials likely diffuse to the high vacancy concentration region around the precipitate and induce abnormal growth. In bulk implanted sample, the weak surface effect results in a similar number of interstitials and vacancies, and they are easily recombined, thus the concentration of vacancies is much lower than that in the thin foil irradiation. Therefore, the vacancies does not interact strongly with precipitates in this case.

Fe precipitates with N-W OR are also unstable under irradiation [28]. Obvious halos appear around the precipitates, and the number density of the precipitates decreases sharply. As shown in Fig. 5(b), the Fe element in halo shows a gradual distribution, which indicates a short range elements redistribution around Fe precipitates. The vacancy formation energy ( $E_{\text{Cu}}^f = 1.23\text{--}1.33$  eV,  $E_{\text{Fe}}^f = 1.4\text{--}1.85$  eV) and migration energy ( $E_{\text{Cu}}^m = 0.72$  eV,  $E_{\text{Fe}}^m = 0.55\text{--}0.77$  eV) of Cu and Fe are similar, so a large amount of Cu interstitial migrates to the free surface, and the high concentration of Cu vacancies combine with Fe interstitials in thin foil sample [49,61]. The combination of Fe interstitial and Cu vacancy captured by the interface leads to the formation of halo and causes precipitate abnormal growth, as illustrated in Fig. 12(d).

According to Fig. 7, in irradiated thin foil, the variation of the diameter of precipitates with K-S OR is larger than that of other precipitates, and its diameter has a continuous distribution, which means that the precipitates absorb unequal amounts of Fe atoms, as illustrated in Fig. 12(e). The sources of Fe interstitials may have two types: Fe atoms that are not completely precipitated, and Fe atoms are knocked-out from some of the precipitates during irradiation, especially the Fe precipitates with N-W ORs. These free Fe interstitials could be captured by the

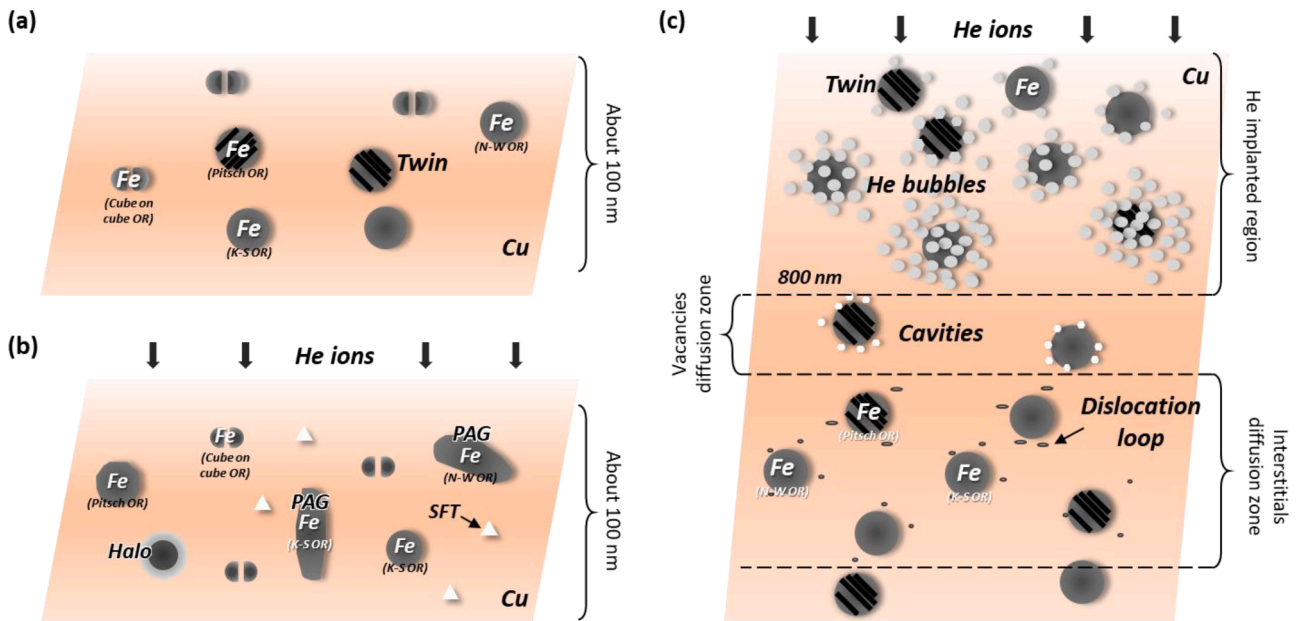


Fig. 11. Schematic of the characteristics of precipitates and irradiation defects in the Cu-1Fe alloy. (a) Four types of precipitate in the as aged Cu-1Fe alloy. (b) Distribution of radiation defects in the irradiated Cu-1Fe alloy after thin foils irradiation. (c) Distribution of radiation defects in the irradiated Cu-1Fe alloy after bulk implantation. PAG is short for precipitate abnormal growth.

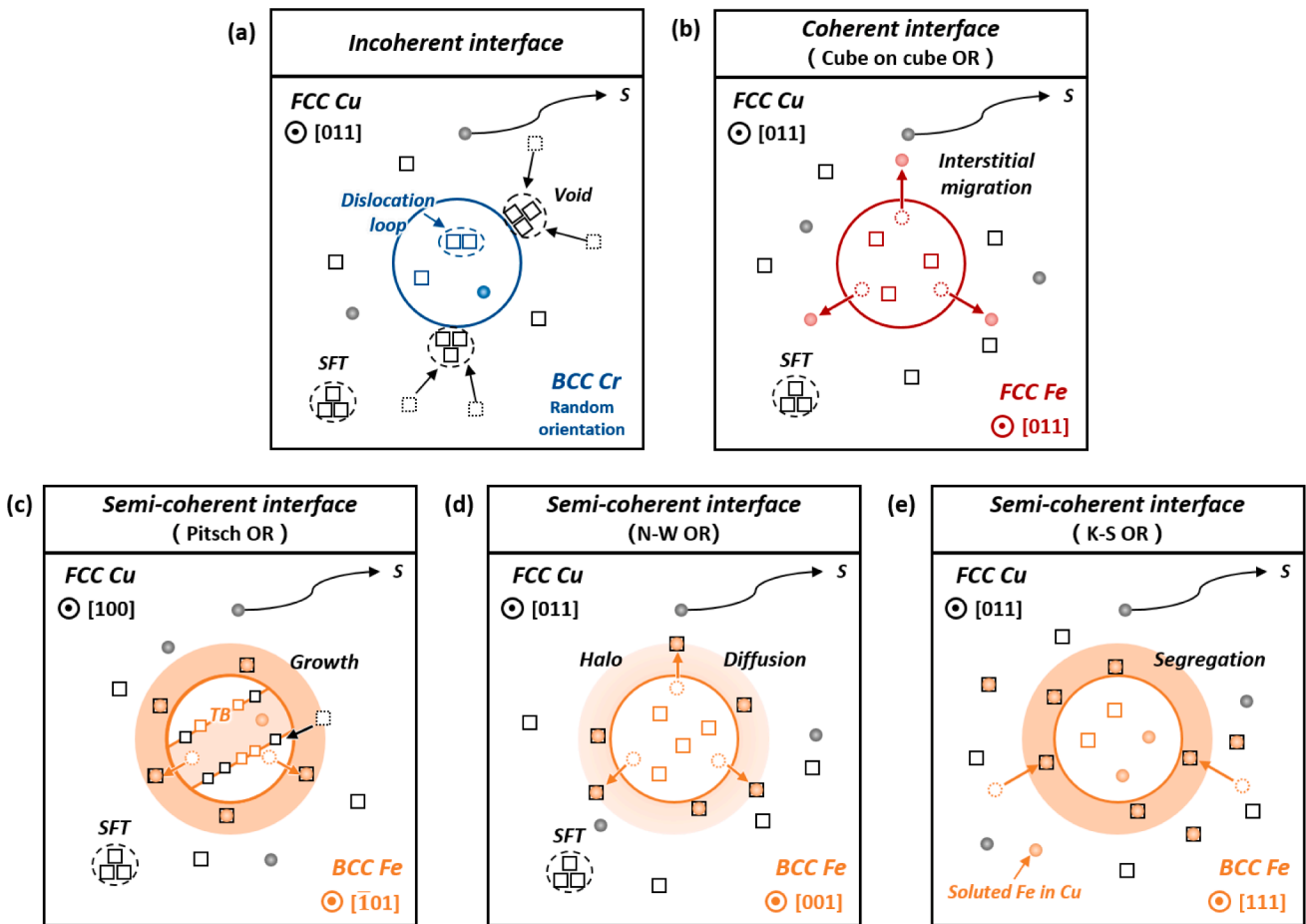


Fig. 12. Schematic of the interaction of point defects with Cu/Cr and Cu/Fe interfaces under thin foil irradiation. (a) Cu vacancies segregate to the Cu/Cr interface. (b) Fe interstitials migrate out of the Fe precipitates with cube on cube OR. (c) Interaction of irradiation-induced point defects with TBs in Fe precipitate with Pitsch OR leads to detwinning. The recombination of Fe interstitials and vacancies at precipitate interface leads to the precipitate growth. (d) Fe interstitials diffuse into the adjacent region of precipitate with N-W OR and form halo. (e) Fe interstitials recombination with vacancies near the precipitates with K-S OR cause precipitate coarsening. Solid balls for interstitials, hollow squares for vacancies, and S for sample surface. The arrows indicate the diffusion direction of point defects.

precipitate with K-S OR, and cause precipitate abnormal growth. Although K-S and N-W OR only have a small difference of  $5.6^\circ$  in interface misorientation, but it has a strong effect on stability of point defects in the Fe precipitates [28]. This is related to the different interface structures in Fe precipitates with K-S or N-W ORs. The K-S interface has two sets of interface dislocations and parallel interface defect arrays, while the N-W interface has seven sets of interface dislocations and triangular interface defect arrays [62,63], the latter is less stable under irradiation.

#### 4.3. Stability of precipitates under irradiation

Among the three types of interfaces, the sink efficiency of the coherent precipitates is the weakest, due to the low mismatch. Under the same irradiation conditions, compared with the semi-coherent Fe precipitates, the Cr precipitates accumulate more serious radiation damage at the incoherent interface-formation of large-sized voids. This is similar to the accumulation of He bubbles at incoherent interfaces in ODS steel after irradiation [33]. This means that the strong sink effect on the point defects may be the intrinsic feature of the incoherent precipitates. However, the semi-coherent Fe precipitates regulate the movement and evolution of point defects in the way of TBs migration, element diffusion and mass transportation, while no large-sized cavity formation under thin foil irradiation. The different interactions behaviors of irradiation defects with precipitates indicate that the semi-coherent precipitates are less likely to accumulate high amount of irradiation defects and have excellent irradiation tolerance. These findings demonstrate that, only increase the number density of precipitates is not enough, one need to consider the character of precipitates in future radiation-resistant materials design. In particular, choosing proper interfaces, for example, abundant semi-coherent interfaces are radiation resistance.

## 5. Conclusions

In this work, we systematically investigated the interaction between irradiation-induced point defects with precipitates in CuCrZr and Cu-1Fe alloys under both thin foil irradiation and He bulk implantation. The key findings are:

- (1) The distribution of voids and He bubbles near Cr precipitates indicates that incoherent precipitates are strong sink and attract large number of vacancies in CuCrZr.
- (2) The FCC Fe precipitate has no obvious change after irradiation, which means that the coherent precipitate interfaces have low sink efficiency due to small lattice mismatch in Cu-1Fe.
- (3) Different types of semi-coherent Fe precipitates exhibit irradiation damage in the form of TBs migration, elemental diffusion and abnormal precipitate growth under thin foil irradiation in Cu-1Fe.
- (4) The coherent, semi-coherent and incoherent Fe precipitates show different sink efficiency, and the semi-coherent BCC Fe precipitates could effectively coordinate the movement and recombination of point defects, thus have a better radiation tolerance in the five types of precipitates in Cu alloy.

## Declaration of Competing Interest

The authors declare that there are no competing financial interests.

## Acknowledgments

This research was supported by the National Natural Science Foundation of China (Grant Nos. 51922082 and 51971170), the 111 Project of China (Grant No BP2018008) and the Shaanxi Science & Technology Innovation Project (Grant No. 2022QFY10-03).

## Supplementary materials

Supplementary material associated with this article can be found, in the online version, at doi:10.1016/j.actamat.2023.118964.

## References

- [1] S.J. Zinkle, Fusion materials science: overview of challenges and recent progress, *Phys. Plasma* 12 (2005), 058101.
- [2] S.J. Zinkle, G.S. Was, Materials challenges in nuclear energy, *Acta Mater.* 61 (2013) 735–758.
- [3] S.J. Zinkle, J.T. Busby, Structural materials for fission & fusion energy, *Mater. Today* 12 (2009) 12–19.
- [4] S.J. Zinkle, L.L. Snead, Designing radiation resistance in materials for fusion energy, *Annu. Rev. Mater. Res.* 44 (2014) 241–267.
- [5] Y. Ueda, K. Schmid, M. Balden, J.W. Coenen, T. Loewenhoff, A. Ito, A. Hasegawa, C. Hardie, M. Porton, M. Gilbert, Baseline high heat flux and plasma facing materials for fusion, *Nucl. Fusion* 57 (2017), 092006.
- [6] S. Tähtinen, M. Pyykkönen, P. Karjalainen-Roikonen, B.N. Singh, P. Toft, Effect of neutron irradiation on fracture toughness behaviour of copper alloys, *J. Nucl. Mater.* 258–263 (1998) 1010–1014.
- [7] S.A. Fabritsiev, S.J. Zinkle, B.N. Singh, Evaluation of copper alloys for fusion reactor divertor and first wall components, *J. Nucl. Mater.* 233–237 (1996) 127–137.
- [8] I.J. Beyerlein, M.J. Demkowicz, A. Misra, B.P. Uberuaga, Defect-interface interactions, *Prog. Mater. Sci.* 74 (2015) 125–210.
- [9] W.Z. Han, M.J. Demkowicz, N.A. Mara, E. Fu, S. Sinha, A.D. Rollett, Y.Q. Wang, J. S. Carpenter, I.J. Beyerlein, A. Misra, Design of radiation tolerant materials via interface engineering, *Adv. Mater.* 25 (2013) 6975–6979.
- [10] S.A. Fabritsiev, A.S. Pokrovsky, Effect of high doses of neutron irradiation on physico-mechanical properties of copper alloys for ITER applications, *Fusion Eng. Des.* 73 (2005) 19–34.
- [11] M.J. Demkowicz, R.G. Hoagland, J.P. Hirth, Interface structure and radiation damage resistance in Cu-Nb multilayer nanocomposites, *Phys. Rev. Lett.* 100 (2008), 136102.
- [12] S.M. Liu, W.Z. Han, Mechanism of interaction between interface and radiation defects in metal, *Acta Phys. Sin.* 68 (2019), 137901.
- [13] M. Wang, I.J. Beyerlein, J. Zhang, W.Z. Han, Defect-interface interactions in irradiated Cu/Ag nanocomposites, *Acta Mater.* 160 (2018) 211–223.
- [14] W.Z. Han, N.A. Mara, Y.Q. Wang, A. Misra, M.J. Demkowicz, He implantation of bulk Cu-Nb nanocomposites fabricated by accumulated roll bonding, *J. Nucl. Mater.* 452 (2014) 57–60.
- [15] J.L. Du, S.H. Jiang, P.P. Cao, C. Xu, Y. Wu, H.Q. Chen, E.G. Fu, Z.P. Lu, Superior radiation tolerance via reversible disordering-ordering transition of coherent superlattices, *Nat. Mater.* 22 (2023) 442–449.
- [16] M. Li, S.J. Zinkle, R.J.M. Konings, 4.20 - Physical and mechanical properties of copper and copper alloys. *Comprehensive Nuclear Materials*, Elsevier, Oxford, 2012, pp. 667–690.
- [17] N. Sekimura, T. Zama, H. Kawanishi, S. Ishino, Precipitate stability in austenitic stainless steels during heavy ion irradiation, *J. Nucl. Mater.* 141–143 (1986) 771–775.
- [18] B.N. Singh, D.J. Edwards, M. Eldrup, P. Toft, Effects of heat treatments and neutron irradiation on microstructures and physical and mechanical properties of copper alloys, *J. Nucl. Mater.* 249 (1997) 1–16.
- [19] M. Hatakeyama, T. Toyama, J. Yang, Y. Nagai, M. Hasegawa, T. Ohkubo, M. Eldrup, B.N. Singh, 3D-AP and positron annihilation study of precipitation behavior in Cu-Cr-Zr alloy, *J. Nucl. Mater.* 386–388 (2009) 852–855.
- [20] N. Gao, T. Tiainen, Y. Ji, L. Laakso, Control of microstructures and properties of a phosphorus-containing Cu-0.6 wt.% Cr alloy through precipitation treatment, *J. Mater. Eng. Perform.* 9 (2000) 623–629.
- [21] T. Fujii, H. Nakazawa, M. Kato, U. Dahmen, Crystallography and morphology of nanosized Cr particles in a Cu-0.2% Cr alloy, *Acta Mater.* 48 (2000) 1033–1045.
- [22] J. Wang, H.T. Zhang, H.D. Fu, J.X. Xie, Effect of Cr content on microstructure and properties of aged Cu-Cr-P alloys, *Trans. Nonferrous Met. Soc. China* 31 (2021) 232–242.
- [23] C.P. Luo, U. Dahmen, Interface structure of faceted lath-shaped Cr precipitates in a Cu-0.33 wt% Cr alloy, *Acta Mater.* 46 (1998) 2063–2081.
- [24] I.S. Batra, G.K. Dey, U.D. Kulkarni, S. Banerjee, Microstructure and properties of a Cu-Cr-Zr alloy, *J. Nucl. Mater.* 299 (2001) 91–100.
- [25] C.P. Luo, U. Dahmen, K.H. Westmacott, Morphology and crystallography of Cr precipitates in a Cu-0.33 wt% Cr alloy, *Acta Metall. Mater.* 42 (1994) 1923–1932.
- [26] Z.G. Wang, G.M. Cao, W.N. Zhang, C.G. Li, Z.Y. Liu, Nucleation and growth of nanoscale precipitates and the effect on properties during secondary isothermal aging in thin-band of Cu-0.8Cr-0.1Zr alloy, *Material* 23 (2022), 101452.
- [27] Q.Y. Dong, M.P. Wang, L.N. Shen, Y.L. Jia, Z. Li, Diffraction analysis of  $\alpha$ -Fe precipitates in a polycrystalline Cu-Fe alloy, *Mater. Charact.* 105 (2015) 129–135.
- [28] U. Dahmen, Orientation relationships in precipitation systems, *Acta Metall.* 30 (1982) 63–73.
- [29] N. Ishikawa, A. Sato, *In-situ* observation of  $\gamma \rightarrow \alpha$  transformation of Fe particles in a Cu-Fe alloy, *Philos. Mag. A* 64 (2006) 387–394.
- [30] M. Kato, R. Monzen, T. Mori, A stress-induced martensitic transformation of spherical iron particles in a CuFe alloy, *Acta Metall.* 26 (1978) 605–613.
- [31] A. Sato, N. Ishikawa, T. Mori, Nucleation and growth of defect clusters in an electron-irradiated Cu-Fe alloy, *Mater. Sci. Eng.* 81 (1986) 427–432.

- [32] N. Ishikawa, A. Sato, Formation of stacking fault tetrahedra around Fe particles in a Cu-Fe alloy, *Philos. Mag. Lett.* 60 (1989) 255–259.
- [33] L. Hsiung, M. Fluss, S. Tumey, J. Kuntz, B. El-Dasher, M. Wall, B. Choi, A. Kimura, F. Willaime, Y. Serruys, HRTEM study of oxide nanoparticles in K3-ODS ferritic steel developed for radiation tolerance, *J. Nucl. Mater.* 409 (2011) 72–79.
- [34] P. Song, D. Morrall, Z.X. Zhang, K. Yabuuchi, A. Kimura, Radiation response of ODS ferritic steels with different oxide particles under ion-irradiation at 550 °C, *J. Nucl. Mater.* 502 (2018) 76–85.
- [35] N. Ishikawa, A. Sato, Effect of an internal stress on formation of stacking fault tetrahedra in an electron-irradiated Cu-Fe alloy, *Philos. Mag. A* 61 (1990) 929–941.
- [36] Z.C. Li, Dose and dose rate effects on coherent-to-incoherent transition of precipitates upon irradiation, *Rare Met.* 25 (2006) 328–332.
- [37] G.R. Woolhouse, M. Ipohorski, On the interaction between radiation damage and coherent precipitates, *Proc. R. Soc. Lond. A* 324 (1971) 415–431.
- [38] W.V. Vaidya, Modification of the precipitate interface under irradiation and its effect on the stability of precipitates, *J. Nucl. Mater.* 83 (1979) 223–230.
- [39] J.P. Wharry, M.J. Swenson, K.H. Yano, A review of the irradiation evolution of dispersed oxide nanoparticles in the b.c.c. Fe-Cr system: current understanding and future directions, *J. Nucl. Mater.* 486 (2017) 11–20.
- [40] D. Watanabe, C. Watanabe, R. Monzen, Determination of the interface energies of spherical, cuboidal and octahedral face-centered cubic precipitates in Cu-Co, Cu-Co-Fe and Cu-Fe alloys, *Acta Mater.* 57 (2009) 1899–1911.
- [41] Y.L. He, S. Godet, J.J. Jonas, Representation of misorientations in Rodrigues-Frank space: application to the Bain, Kurdjumov-Sachs, Nishiyama-Wassermann and Pitsch orientation relationships in the Gibeon meteorite, *Acta Mater.* 53 (2005) 1179–1190.
- [42] J.F. Ziegler, J.P. Biersack, U. Littmark, *The Stopping and Range of Ions in Solids*, Ion Implantation Science and Technology, Pergamon Press, New York, 1985.
- [43] M. Nastasi, J.W. Mayer, J.K. Hirvonen, *Ion-Solid Interactions - Fundamentals and Applications*, Cambridge University Press, Cambridge, 1996.
- [44] M.J. Tenwick, H.A. Davies, Enhanced strength in high conductivity copper alloys, *Mat. Sci. Eng.* 98 (1988) 543–546.
- [45] N.Y. Tang, D.M.R. Taplin, G.L. Dunlop, Precipitation and aging in high conductivity Cu-Cr alloys with additions of zirconium and magnesium, *Mater. Sci. Technol.* 1 (1985) 270–275.
- [46] J.M. Zhang, F. Ma, K.W. Xu, Calculation of the surface energy of bcc metals by using the modified embedded-atom method, *Surf. Interface Anal.* 35 (2003) 662–666.
- [47] Y.N. Wen, J.M. Zhang, Surface energy calculation of the bcc metals by using the MAEAM, *Comput. Mater. Sci.* 42 (2008) 281–285.
- [48] Y.N. Wen, J.M. Zhang, Surface energy calculation of the fcc metals by using the MAEAM, *Solid State Commun.* 144 (2007) 163–167.
- [49] R.W. Balluffi, Vacancy defect mobilities and binding energies obtained from annealing studies, *J. Nucl. Mater.* 69–70 (1978) 240–263.
- [50] L.M. Wei, Y.G. Li, G.G. Zhao, Q.R. Zheng, J.W. Li, Z. Zeng, Key factors in radiation tolerance of BCC metals under steady state, *Nucl. Instrum. Methods Phys. Res. Sect. B* 455 (2019) 134–139.
- [51] J.P. Hirth, J. Lothe, T. Mura, Theory of dislocations, *J. Appl. Mech.* 50 (1983) 476.
- [52] M.G. Hall, H.I. Aaronson, K.R. Kinsma, Structure of nearly coherent fcc: bcc boundaries in a Cu-Cr alloy, *Surf. Sci.* 31 (1972) 257–274.
- [53] C. Michaelsen, C. Gente, R. Bormann, Phase formation and thermodynamics of unstable Cu-Cr alloys, *J. Mater. Res. Technol.* 12 (1997) 1463–1467.
- [54] Z.S. Basinski, W. Hume-Rothery, A.L. Sutton, The lattice expansion of iron, *Proc. R. Soc. Lond. Math. Phys. Sci.* 229 (1954) 459–467.
- [55] R.W.G. Wyckoff, *Crystal Structures*, Interscience Publishers, New York, London, Sydney, 1965.
- [56] W.Z. Han, M.J. Demkowicz, E.G. Fu, Y.Q. Wang, A. Misra, Effect of grain boundary character on sink efficiency, *Acta Mater.* 60 (2012) 6341–6351.
- [57] J. Marian, B.D. Wirth, J.M. Perlado, G.R. Odette, T.D.D.L. Rubia, Dynamics of self-interstitial migration in Fe-Cu alloys, *Phys. Rev. B* 64 (2001) 94303.
- [58] K.Y. Yu, D. Bufford, F. Khatkhatay, H. Wang, M.A. Kirk, X. Zhang, *In situ* studies of irradiation-induced twin boundary migration in nanotwinned Ag, *Scr. Mater.* 69 (2013) 385–388.
- [59] C. Fan, J. Li, Z. Fan, H. Wang, X. Zhang, *In situ* studies on the irradiation-induced twin boundary-defect interactions in Cu, *Metall. Mater. Trans. A* 48 (2017) 5172–5180.
- [60] D.K. Song, X.G. Li, J.M. Xue, H.L. Duan, Z.H. Jin, Irradiation-enhanced twin boundary migration in BCC Fe, *Philos. Mag. Lett.* 94 (2014) 361–369.
- [61] I. Valikova, A. Nazarov, Simulation of atomic structure and diffusion characteristics of point defects in BCC and FCC metals, *Solid State Phenom.* 172–174 (2011) 1222–1227.
- [62] J. Wang, R.F. Zhang, C.Z. Zhou, L.J. Beyerlein, A. Misra, Interface dislocation patterns and dislocation nucleation in face-centered-cubic and body-centered-cubic bicrystal interfaces, *Int. J. Plast.* 53 (2014) 40–55.
- [63] J.N. Hu, H.T. Zhang, Y.L. Zhu, P.B. Li, G.Q. Luo, C.B. Wang, Q. Shen, L.M. Zhang, Molecular dynamics simulation of tensile deformation of nanometer multilayer Cu-Ta materials, *Mater. Technol.* 56 (2022) 415–422.